AIAA JOURNAL
Vol. 49, No. 7, July 2011

High-Order Interpolation Method for Overset Grid Based on Finite Volume Method

Kyung Rock Lee,* Jung Ho Park,† and Kyu Hong Kim‡
Seoul National University, Seoul 151-742, Republic of Korea

DOI: 10.2514/1.J050620

To enhance accuracy in a high-order flow solver with an overset grid method, a high-order interpolation method was developed based on finite volume method in the Euler equations. To improve stability when calculating a nonlinear discontinuity with the high-order interpolation, the interpolation was combined with a multidimensional limiting process to remove oscillatory phenomena. Thus, the proposed method can be robustly applied to a discontinuous region as well as a continuous one. It was compared with conventional methods using test cases, thereby verifying its accuracy and efficiency. It can be extendable to the Navier–Stokes equations without any modification, even though it was tested in the Euler equations in the present paper.

Nomenclature

e, e_t	=	internal energy, total energy
M	=	Mach number
p	=	pressure
u, v	=	velocity in the x, y direction
x, y	=	physical domain
ξ, η	=	computational domain
ρ	=	density
Φ	=	point value of property Φ
$\bar{\Phi}$	=	cell-averaged value of property Φ

I. Introduction

THE grid-generation method is a key issue in computational fluid dynamics. The overset grid method Chimera [1] has been developed over the last two decades to analyze the flowfields of complex or moving geometries [2,3]. The overset grid method has many advantages in the analysis of complex geometry and moving systems that are difficult to realize using a single structured grid. Also, it is easier to modify local parts of the geometry when complex geometry is changed, because no effort is needed to regenerate the entire grid system except the changed parts. In this method, overlapping grids are calculated independently, and communication between them is performed by exchanging variables of the flow.

The overset grid method has two steps. The first step is a hole-cutting process, to remove mesh points that are not needed for calculations within a solid body from the computational domain. To improve the efficiency of this process, various hole-cutting methods have been developed by Chiu and Meakin [4], Meakin [5], and Wang et al. [6]. The purpose of the second step is to update the values of the fringe cells, using an interpolation algorithm. To improve the accuracy of the interpolation process, Wang [7] and Zheng and Liou [8] discussed conservative interpolation algorithms. Yin and Delfs [9], Delfs [10], and Sherer and Scott [11] demonstrated the use of an overset grid method with a high-order algorithm based on the finite difference method (FDM).

In this study, we focused on the high-order interpolation method. When a second-order flow solver is used, linear interpolation is mainly used as the interpolation method. In many cases, a second-order flow solver is adequate to analyze fluid flows. However, a high-order flow solver is useful to calculate high-frequency problems such as turbulence, aeroacoustics, and electromagnetics, because it has advantages over a low-order flow solver to calculate high-frequency phenomena correctly. When a conventional linear interpolation is applied to the high-order flow solver in a real calculation, the accuracy of the solution is affected, especially for unsteady problems. Thus, to satisfy high-order accuracy, high-order interpolation is necessary for the overset grid method [12]. Recent studies on the high-order interpolation methods are weighted toward FDM [9–11] and usually solve the continuous problem. They were not enough to calculate problems with coexisting nonlinear and linear characteristics, such as shock–vortex interaction. Thus, a high-order interpolation method that can address these problems is required. We developed a method that can provide high-order resolution in problems with nonlinear and linear characteristics.

The proposed interpolation method consists of two parts. First, the high-order interpolation based on finite volume method (FVM) was developed for the overset grid method. Second, a multidimensional limiting process (MLP) [13] is applied to the proposed interpolation to remove oscillations in discontinuous regions. High-order interpolation generally produces oscillation near discontinuous regions, which has a negative effect on the stability of the solution. Therefore, to enhance the stability of the proposed interpolation, the MLP was applied to the high-order interpolation for the overset grid method.

The paper is organized as follows. After a description of the governing equations and flow solver in Sec. II, the high-order interpolation based on the FVM is described in Sec. III. The use of the MLP to remove oscillatory phenomena is introduced in Sec. IV. In Sec. V, numerical test cases are presented to verify the accuracy and efficiency of the proposed interpolation method. Finally, our conclusions are given in Sec. VI.

II. Governing Equations

The two-dimensional Euler equations in conservative form are given as follows:

$$\int \frac{\partial \mathbf{Q}}{\partial t}\,d\mathbf{V} + \int \frac{\partial \mathbf{E}}{\partial x}\,d\mathbf{V} + \int \frac{\partial \mathbf{F}}{\partial y}\,d\mathbf{V} = 0 \tag{1}$$

where the solution vectors $\mathbf{Q}$ and the flux vectors $\mathbf{E}$ and $\mathbf{F}$ are given by

Presented as Paper 2009-3660 at the 19th AIAA Computational Fluid Dynamics, San Antonio, TX, 22–25 June 2009; received 22 April 2010; revision received 17 January 2011; accepted for publication 20 January 2011.

*Ph.D. Candidate, School of Mechanical and Aerospace Engineering, Building 40, San 56-1, Shinlim-dong, Gwanak-gu; rudfhr1228@hanmail.net.

†Ph.D. Candidate, School of Mechanical and Aerospace Engineering, Building 40, San 56-1, Shinlim-dong, Gwanak-gu; ultima18@snu.ac.kr.

‡Associate Professor, School of Mechanical and Aerospace Engineering and Institute of Advanced Aerospace Technology, Building 302-628, San 56-1, Shinlim-dong, Gwanak-gu; aerocfd1@snu.ac.kr. Member AIAA (Corresponding Author).

$$\mathbf{Q} = \begin{bmatrix} \rho \\ \rho u \\ \rho v \\ \rho e_t \end{bmatrix}, \quad \mathbf{E} = \begin{bmatrix} \rho u \\ \rho u^2 + p \\ \rho uv \\ (\rho e_t + p)u \end{bmatrix}, \quad \mathbf{F} = \begin{bmatrix} \rho v \\ \rho uv \\ \rho v^2 + p \\ (\rho e_t + p)v \end{bmatrix} \tag{2}$$

The equation of state for a calorically perfect gas is given by

$$p = (\gamma - 1)\rho e = (\gamma - 1)\rho\left(e_t - \frac{1}{2}(u^2 + v^2)\right) \tag{3}$$

where $\gamma = 1.4$ for air.

III. High-Order Interpolation Based on Finite Volume Method for Overset Grid Method

An interpolation for the overset grid method has two subprocesses. One is the interpolation process from grid 1 to grid 2, as shown in Fig. 1a; the other is from grid 2 to grid 1, as shown in Fig. 1b. The dark cells in Figs. 1a and 1b indicate interpolation points for each process. Because both processes use the same interpolation method, the explanation of the proposed method is based on the process from grid 1 to grid 2 in the present paper.

A. Bilinear Interpolation Method

A bilinear interpolation method is widely used in the second-order flow solvers. The interpolated value of fringe cell 1 in grid 2, by the bilinear interpolation method $\bar{\Phi}$, can be obtained as follows:

$$\bar{\Phi} = A\xi_1 + B\eta_1 + C\xi_1\eta_1 + D \tag{4}$$

where (ξ_1, η_1) is the location of the cell center point of fringe cell 1, as shown in Fig. 2.

To obtain this function, four stencil cells (S_1, S_2, S_3, S_4) in grid 1 are needed. Even though $\bar{\Phi}_{i,j}$, $\bar{\Phi}_{i+1,j}$, $\bar{\Phi}_{i,j+1}$, and $\bar{\Phi}_{i+1,j+1}$ are the cell-averaged values of stencil cells originally, these are treated like point values at cell center point in the bilinear interpolation method. Then, the interpolated value $\bar{\Phi}$ by Eq. (4) is considered as the cell-averaged value. Coefficients A, B, C, and D in Eq. (4) can be obtained as

$$A = \bar{\Phi}_{i+1,j} - \bar{\Phi}_{i,j}, \qquad B = \bar{\Phi}_{i,j+1} - \bar{\Phi}_{i,j}$$
$$C = \bar{\Phi}_{i,j} - \bar{\Phi}_{i+1,j} - \bar{\Phi}_{i,j+1} + \bar{\Phi}_{i+1,j+1}, \qquad D = \bar{\Phi}_{i,j} \tag{5}$$

B. Fourth-Order Interpolation Based on Finite Volume Method

In this study, the fourth-order interpolation method based on FVM was introduced to obtain the cell-averaged value of fringe cell $\bar{\Phi}_o$ in grid 2. The donor cell of grid 1, in which the fringe cell center of grid 2 is located, must be searched, as shown in Fig. 3. The dashed line represents the fringe cell in grid 2, and the solid line represents the donor cell in grid 1, as shown in Fig. 3b. In the figure, point (x_m, y_m) is the origin of the donor cell, and point (x_o, y_o) is the origin of the fringe cell. Each Δx, Δy means the distance between (x_m, y_m) and (x_o, y_o).

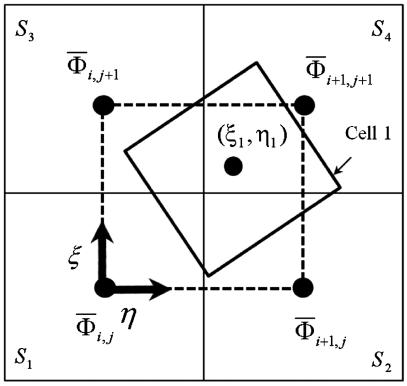

Fig. 2 Schematic of bilinear interpolation method.

The fourth-order interpolation process for $\bar{\Phi}_o$ is divided into three steps, as shown in Fig. 4:

1) Find the fourth-order interpolation function in grid 1. In step 1, stencil cells are determined as the 10 nearest cells from the fringe cell, and the interpolation function in grid 1 in terms of the coordinates (ξ_m, η_m) is obtained as shown in Fig. 4a.

2) Transform the coordinates from grid 1 to grid 2:

$$\Phi_m(\xi_m, \eta_m) \rightarrow \Phi_o(\xi_o, \eta_o)$$

Step 2 is introduced to follow the FVM concept rigorously. As shown in Fig. 4b, the interpolation function $\Phi_m(\xi_m, \eta_m)$ in grid 1 through step 1 is expressed in terms of coordinates of grid 2, (ξ_o, η_o). Throughout this step, the integration of the interpolation function $\Phi_o(\xi_o, \eta_o)$ inside a cell can be easily performed in an arbitrary overset grid system.

3) Obtain the cell-averaged value of the fringe cell in grid 2. In step 3, $\Phi_o(\xi_o, \eta_o)$ is integrated to obtain a cell-averaged value $\bar{\Phi}_o$ in the fringe cell. The details of each step are explained in the following sections.

1. *Step 1: Find the Fourth-Order Interpolation Function in Grid 1*

Step 1: the fourth-order interpolation function of ξ_m, η_m in grid 1 is given by

$$\Phi_m(\xi_m, \eta_m) = A\xi_m^3 + B\eta_m^3 + C\xi_m^2\eta_m + D\xi_m\eta_m^2 + E\xi_m^2 + F\eta_m^2 + G\xi_m\eta_m + H\xi_m + I\eta_m + J \tag{6}$$

This function is obtained in two steps.

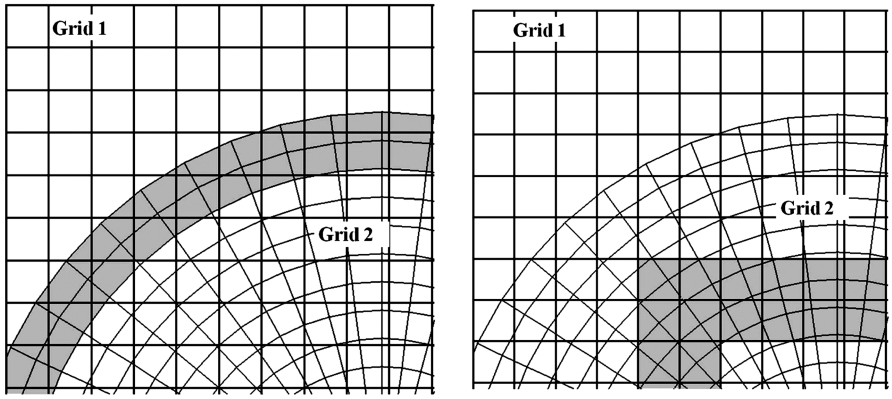

a) Interpolation points in Grid 2 **b) Interpolation points in Grid 1**

Fig. 1 Overset grid method.

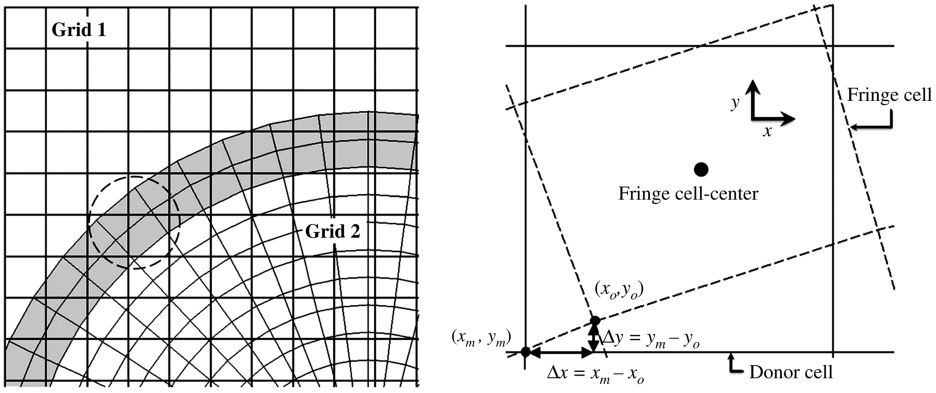

a) Interpolation points in Grid 2 **b) Physical domain**

Fig. 3 Coordinate for each grid.

Step 1-1: select the 10 nearest cells from the fringe cell as stencil cells for the fourth-order interpolation function. There are four cases according to the location of the fringe cell center (point c) in the donor cell. The location is determined by comparing the distance (l_1, l_2, l_3, l_4) between point c and each vertex (P_1, P_2, P_3, P_4) of the donor cell, as shown in Fig. 5. Each case is shown in Fig. 6, according to the fringe cell location:

$$\text{Minimum } (l_1, l_2, l_3, l_4) = \begin{cases} l_1 \rightarrow \text{case 1} \\ l_2 \rightarrow \text{case 2} \\ l_3 \rightarrow \text{case 3} \\ l_4 \rightarrow \text{case 4} \end{cases}$$

If two or more of l_1, l_2, l_3, l_4 are equal as minimum value, the case of the lowest number is selected in the present paper; for example, $l_2 = l_3 < l_1, l_4 \rightarrow$ case 2. Our selection of stencil cases does not affect the accuracy of the solution, because the error of each case has the same order of magnitude $\mathcal{O}(\Delta x^4)$.

When the fringe cell center is located in the domain boundary of grid 1, stencil cells can be selected as follows to avoid requiring additional boundary cells:

1) When the fringe cell center is located in corner cells 1, 2, 3, and 4 of grid 1, stencil cells are selected as cases 1, 2, 3, and 4, respectively, as shown in Fig. 7.

2) When the fringe cell center is located in side boundary cells A, B, C, and D of grid 1, stencil cells are selected between two cases by comparing the distances from the fringe cell center, as follows:

Side A:

$$\text{Minimum } (l_1, l_2) = \begin{cases} l_1 \rightarrow \text{case 1} \\ l_2 \rightarrow \text{case 2} \end{cases}$$

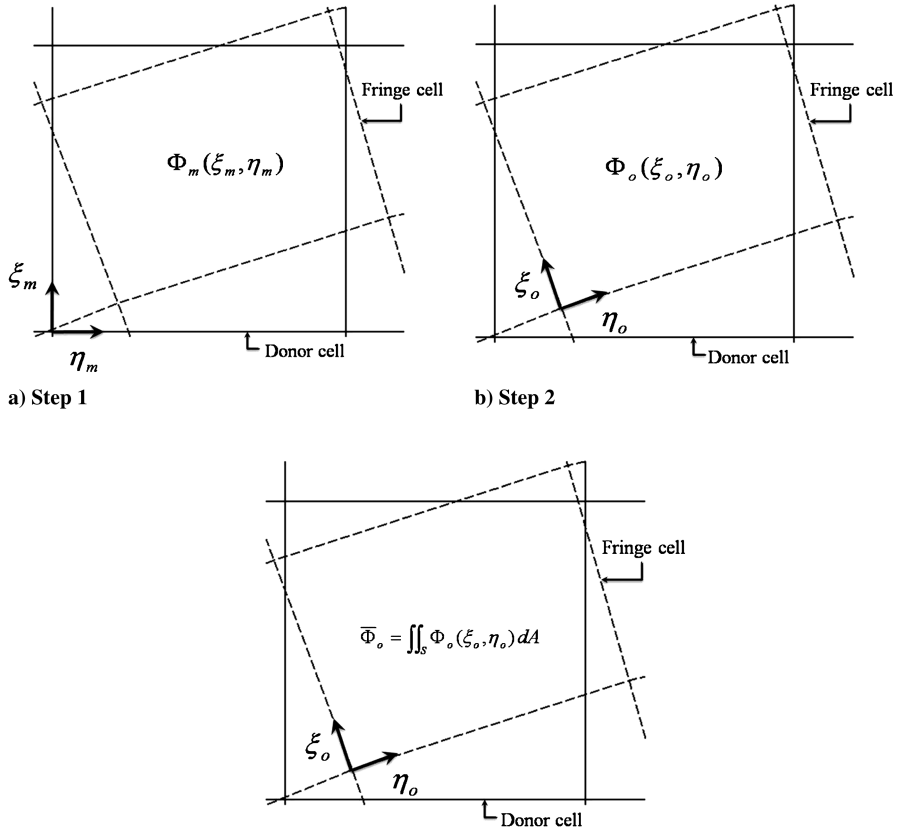

a) Step 1 **b) Step 2**

c) Step 3

Fig. 4 Interpolation process.

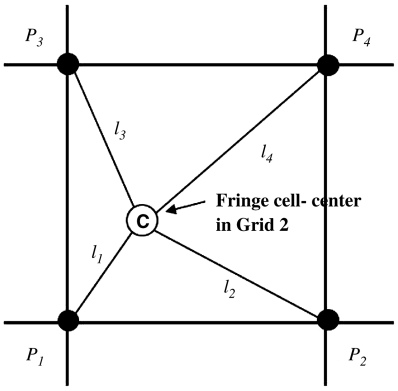

Fig. 5 Distinguish location of the fringe cell center.

Side B:

$$\text{Minimum } (l_1, l_3) = \begin{cases} l_1 \rightarrow \text{case 1} \\ l_3 \rightarrow \text{case 3} \end{cases}$$

Side C:

$$\text{Minimum } (l_3, l_4) = \begin{cases} l_3 \rightarrow \text{case 3} \\ l_4 \rightarrow \text{case 4} \end{cases}$$

Side D:

$$\text{Minimum } (l_2, l_4) = \begin{cases} l_2 \rightarrow \text{case 2} \\ l_4 \rightarrow \text{case 4} \end{cases}$$

Step 1-2: obtain the unknown coefficients in Eq. (6), using the stencil cells chosen previously. Our description is based on case 1, because other cases show rotating forms of case 1 and can be calculated in the same way.

Each stencil cell satisfies Eq. (7), as follows:

$$\bar{\Phi}_m = \int_{\eta_i}^{\eta_{i+1}} \int_{\xi_i}^{\xi_{i+1}} \Phi_m(\xi_m, \eta_m)\, \mathrm{d}\xi_m\, \mathrm{d}\eta_m \tag{7}$$

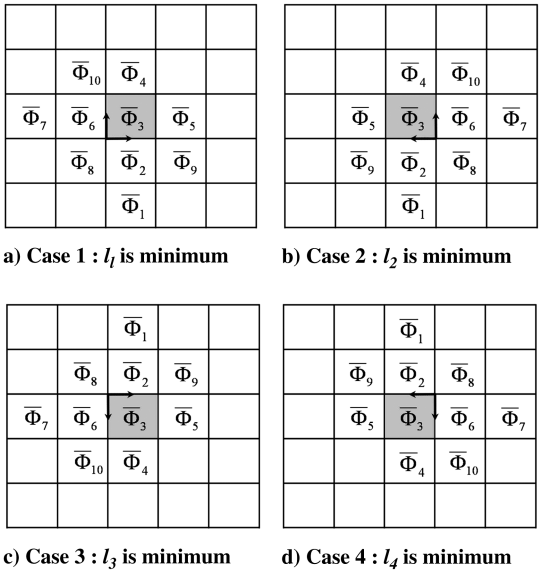

a) Case 1 : l_1 is minimum **b) Case 2 : l_2 is minimum**

c) Case 3 : l_3 is minimum **d) Case 4 : l_4 is minimum**

Fig. 6 Ten stencil cells for each case.

2. Transform Coordinates from Grid 1 to Grid 2

Step 2: to obtain the cell-averaged value of fringe cell $\bar{\Phi}_o$, the function for grid 2, written as Eq. (10), must be obtained. We used a coordinate transformation from grid 1, (ξ_m, η_m), to grid 2, (ξ_o, η_o):

$$\Phi_o(\xi_o, \eta_o) = A'\xi_o^3 + B'\eta_o^3 + C'\xi_o^2\eta_o + D'\xi_o\eta_o^2 + E'\xi_o^2 + F'\eta_o^2 + G'\xi_o\eta_o + H'\xi_o + I'\eta_o + J' \tag{10}$$

The coordinate transformation process is as follows. By the chain rule,

$$x_o = \frac{\partial x_o}{\partial \xi_o}\xi_o + \frac{\partial x_o}{\partial \eta_o}\eta_o \qquad y_o = \frac{\partial y_o}{\partial \xi_o}\xi_o + \frac{\partial y_o}{\partial \eta_o}\eta_o \tag{11}$$

Equation (7) can be rewritten in matrix form, as follows:

$$\begin{bmatrix} \bar{\Phi}_1 \\ \bar{\Phi}_2 \\ \bar{\Phi}_3 \\ \bar{\Phi}_4 \\ \bar{\Phi}_5 \\ \bar{\Phi}_6 \\ \bar{\Phi}_7 \\ \bar{\Phi}_8 \\ \bar{\Phi}_9 \\ \bar{\Phi}_{10} \end{bmatrix} = \begin{bmatrix} 1/4 & -15/4 & -1/2 & 7/6 & 1/3 & 7/3 & -3/4 & 1/2 & -3/2 & 1 \\ 1/4 & -1/4 & -1/6 & 1/6 & 1/3 & 1/3 & -1/4 & 1/2 & -1/2 & 1 \\ 1/4 & 1/4 & 1/6 & 1/6 & 1/3 & 1/3 & 1/4 & 1/2 & 1/2 & 1 \\ 1/4 & 15/4 & 1/2 & 7/6 & 1/3 & 7/3 & 3/4 & 3/2 & 3/2 & 1 \\ 15/4 & 1/4 & 7/6 & 1/2 & 7/3 & 1/3 & 3/4 & 1/2 & 1/2 & 1 \\ -1/4 & 1/4 & 1/6 & -1/6 & 1/3 & 1/3 & -1/4 & -1/2 & 1/2 & 1 \\ -15/4 & 1/4 & 7/6 & -1/2 & 7/3 & 1/3 & -3/4 & -3/2 & 1/2 & 1 \\ -1/4 & -1/4 & -1/6 & -1/6 & 1/3 & 1/3 & 1/4 & -1/2 & -1/2 & 1 \\ 15/4 & -1/4 & -7/6 & 1/2 & 7/3 & 1/3 & -3/4 & 3/2 & -1/2 & 1 \\ -1/4 & 15/4 & 1/2 & -7/6 & 1/3 & 7/3 & -3/4 & -1/2 & 3/2 & 1 \end{bmatrix} \begin{bmatrix} A \\ B \\ C \\ D \\ E \\ F \\ G \\ H \\ I \\ J \end{bmatrix} \tag{8}$$

Then, the coefficients are obtained by inverse transformation:

$$\begin{bmatrix} A \\ B \\ C \\ D \\ E \\ F \\ G \\ H \\ I \\ J \end{bmatrix} = \begin{bmatrix} 0 & 0 & -1/2 & 0 & 1/6 & 1/2 & -1/6 & 0 & 0 & 0 \\ -1/6 & 1/2 & -1/2 & 1/6 & 0 & 0 & 0 & 0 & 0 & 0 \\ 0 & 1 & -1 & 0 & 1/2 & 1/2 & 0 & -1/2 & -1/2 & 0 \\ 0 & 1/2 & -1 & 1/2 & 0 & 1 & 0 & -1/2 & 0 & -1/2 \\ 0 & -1/2 & 1/4 & 0 & 0 & -1/2 & 1/4 & 1/4 & 1/4 & 0 \\ 1/4 & -1/2 & 1/4 & 0 & 0 & -1/2 & 0 & 1/4 & 0 & 1/4 \\ 0 & -1 & 1 & 0 & 0 & -1 & 0 & 1 & 0 & 0 \\ 0 & 1/3 & 13/12 & -1/6 & -1/12 & -13/12 & 1/12 & -1/3 & 0 & 1/6 \\ 1/12 & -13/12 & 13/12 & -1/12 & -1/6 & 1/3 & 0 & -1/3 & 1/6 & 0 \\ -1/12 & 7/12 & 1/12 & 0 & 0 & 7/12 & -1/12 & 1/12 & -1/12 & -1/12 \end{bmatrix} \begin{bmatrix} \bar{\Phi}_1 \\ \bar{\Phi}_2 \\ \bar{\Phi}_3 \\ \bar{\Phi}_4 \\ \bar{\Phi}_5 \\ \bar{\Phi}_6 \\ \bar{\Phi}_7 \\ \bar{\Phi}_8 \\ \bar{\Phi}_9 \\ \bar{\Phi}_{10} \end{bmatrix} \tag{9}$$

The interpolation function for grid 1 was obtained by substituting the coefficients in Eq. (9) into Eq. (6).

$$\xi_m = \frac{\partial \xi_m}{\partial x_m} x_m + \frac{\partial \xi_m}{\partial y_m} y_m \qquad \eta_m = \frac{\partial \eta_m}{\partial x_m} x_m + \frac{\partial \eta_m}{\partial y_m} y_m \tag{12}$$

(x_m, y_m) and (x_o, y_o) have the following relation:

$$x_m = x_o + \Delta x \qquad y_m = y_o + \Delta y \tag{13}$$

Substituting Eq. (11) into Eq. (13) yields

$$x_m = \frac{\partial x_o}{\partial \xi_o} \xi_o + \frac{\partial x_o}{\partial \eta_o} \eta_o + \Delta x \qquad y_m = \frac{\partial y_o}{\partial \xi_o} \xi_o + \frac{\partial y_o}{\partial \eta_o} \eta_o + \Delta y \tag{14}$$

ξ_m and η_m can be expressed as functions of ξ_o and η_o, by substituting Eq. (14) into Eq. (12):

$$\xi_m = \alpha_1 \xi_o + \beta_1 \eta_o + \gamma_1 \qquad \eta_m = \alpha_2 \xi_o + \beta_2 \eta_o + \gamma_2 \tag{15}$$

where α_1, β_1, γ_1, α_2, β_2, and γ_2 are as follows:

$$\alpha_1 = \frac{\partial \xi_m}{\partial x_m}\frac{\partial x_o}{\partial \xi_o} + \frac{\partial \xi_m}{\partial y_m}\frac{\partial y_o}{\partial \xi_o} \qquad \beta_1 = \frac{\partial \xi_m}{\partial x_m}\frac{\partial x_o}{\partial \eta_o} + \frac{\partial \xi_m}{\partial y_m}\frac{\partial y_o}{\partial \eta_o}$$
$$\gamma_1 = \frac{\partial \xi_m}{\partial x_m}\Delta x + \frac{\partial \xi_m}{\partial y_m}\Delta y \qquad \alpha_2 = \frac{\partial \eta_m}{\partial x_m}\frac{\partial x_o}{\partial \xi_o} + \frac{\partial \eta_m}{\partial y_m}\frac{\partial y_o}{\partial \xi_o}$$
$$\beta_2 = \frac{\partial \eta_m}{\partial x_m}\frac{\partial x_o}{\partial \eta_o} + \frac{\partial \eta_m}{\partial y_m}\frac{\partial y_o}{\partial \eta_o} \qquad \gamma_2 = \frac{\partial \eta_m}{\partial x_m}\Delta x + \frac{\partial \eta_m}{\partial y_m}\Delta y$$

Finally, the coefficients in Eq. (10) were obtained by substituting Eq. (15) into Eq. (6), as follows:

$$\begin{bmatrix} A' \\ B' \\ C' \\ D' \\ E' \\ F' \\ G' \\ H' \\ I' \\ J' \end{bmatrix} = \begin{bmatrix} \alpha_1^3 & \alpha_2^3 & \alpha_1^2\alpha_2 & \alpha_1\alpha_2^2 & 0 & 0 & 0 & 0 & 0 & 0 \\ \beta_1^3 & \beta_2^3 & \beta_1^2\beta_2 & \beta_1\beta_2^2 & 0 & 0 & 0 & 0 & 0 & 0 \\ 3\alpha_1^2\beta_1 & 3\alpha_2^2\beta_2 & 2\alpha_1\alpha_2\beta_1 + \alpha_1^2\beta_2 & 2\alpha_1\alpha_2\beta_2 + \alpha_2^2\beta_1 & 0 & 0 & 0 & 0 & 0 & 0 \\ 3\alpha_1\beta_1^2 & 3\alpha_2\beta_2^2 & 2\beta_1\beta_2\alpha_1 + \alpha_2\beta_1^2 & 2\beta_1\beta_2\alpha_2 + \alpha_1\beta_2^2 & 0 & 0 & 0 & 0 & 0 & 0 \\ 3\alpha_1^2\gamma_1 & 3\alpha_2^2\gamma_2 & 2\alpha_1\alpha_2\gamma_1 + \alpha_1^2\gamma_2 & 2\alpha_1\alpha_2\gamma_2 + \alpha_2^2\gamma_1 & \alpha_1^2 & \alpha_2^2 & \alpha_1\alpha_2 & 0 & 0 & 0 \\ 3\beta_1^2\gamma_1 & 3\beta_2^2\gamma_2 & 2\beta_1\beta_2\gamma_1 + \beta_1^2\gamma_2 & 2\beta_1\beta_2\gamma_2 + \beta_2^2\gamma_1 & \beta_1^2 & \beta_2^2 & \beta_1\beta_2 & 0 & 0 & 0 \\ 6\alpha_1\beta_1\gamma_1 & 6\alpha_2\beta_2\gamma_2 & 2(\alpha_2\beta_1\gamma_1 + \alpha_1\beta_2\gamma_1 + \alpha_1\beta_1\gamma_2) & 2(\alpha_1\beta_2\gamma_2 + \alpha_2\beta_1\gamma_2 + \alpha_2\beta_2\gamma_1) & 2\alpha_1\beta_1 & 2\alpha_2\beta_2 & \alpha_1\beta_2 + \alpha_2\beta_1 & 0 & 0 & 0 \\ 3\alpha_1\gamma_1^2 & 3\alpha_2\gamma_2^2 & 2\gamma_1\gamma_2\alpha_1 + \alpha_2\gamma_1^2 & 2\gamma_1\gamma_2\alpha_2 + \alpha_1\gamma_2^2 & 2\alpha_1\gamma_1 & 2\alpha_2\gamma_2 & \alpha_1\gamma_2 + \alpha_2\gamma_1 & \alpha_1 & \alpha_2 & 0 \\ 3\beta_1\gamma_1^2 & 3\beta_2\gamma_2^2 & 2\gamma_1\gamma_2\beta_1 + \beta_2\gamma_1^2 & 2\gamma_1\gamma_2\beta_2 + \beta_1\gamma_2^2 & 2\beta_1\gamma_1 & 2\beta_2\gamma_2 & \beta_1\gamma_2 + \beta_2\gamma_1 & \beta_1 & \beta_2 & 0 \\ \gamma_1^3 & \gamma_2^3 & \gamma_1^2\gamma_2 & \gamma_1\gamma_2^2 & \gamma_1^2 & \gamma_2^2 & \gamma_1\gamma_2 & \gamma_1 & \gamma_2 & 1 \end{bmatrix} \times \begin{bmatrix} A \\ B \\ C \\ D \\ E \\ F \\ G \\ H \\ I \\ J \end{bmatrix} \tag{16}$$

3. Obtain Cell-Averaged Value of Fringe Cell in Grid 2

Step 3: the cell-averaged value $\bar{\Phi}_o$ was obtained by integrating the function for grid 2, $\Phi_o(\xi_o, \eta_o)$, in Eq. (10). For accurate integration, the fringe cell was divided into two regions, as shown in Fig. 8. Then, two overset interpolation functions, $\Phi_o(\xi_{o,1}, \eta_{o,1})$ and $\Phi_o(\xi_{o,2}, \eta_{o,2})$, were obtained through step 2. $\Phi_o(\xi_{o,1}, \eta_{o,1})$ was transformed by $\xi_{o,1}$, $\eta_{o,1}$ in region 1, and $\Phi_o(\xi_{o,2}, \eta_{o,2})$ was transformed by $\xi_{o,2}$, $\eta_{o,2}$ in region 2. Then, each function is integrated in region 1 and 2, as shown in Fig. 8. Finally, $\bar{\Phi}_o$ was obtained by summing these integrated values:

$$\bar{\Phi}_o = \iint_1 \Phi_o(\xi_{o,1}, \eta_{o,1})\, dA_1 + \iint_2 \Phi_o(\xi_{o,2}, \eta_{o,2})\, dA_2 \tag{17}$$

IV. Multidimensional Limiting Process for Overset Grid Method

If an overlapping grid is located in a discontinuous region, it is highly probable that the interpolated value from Eq. (17) will lead to oscillatory behaviors as well. To avoid this problem, an oscillation removal process, MLP [13], was applied in the interpolation.

The MLP has two steps: 1) the distinguishing mechanism (distinguishing between a continuous and a discontinuous region) and 2) the application of the MLP (if the fringe cell is determined to be located in a discontinuous region).

A. Step 1: Distinguishing Mechanism

A distinguishing mechanism between a continuous and a discontinuous region is essential, to preserve the high-order accuracy in a continuous region and to perform stable calculation in a discontinuous region. However, it is not obvious how to distinguish

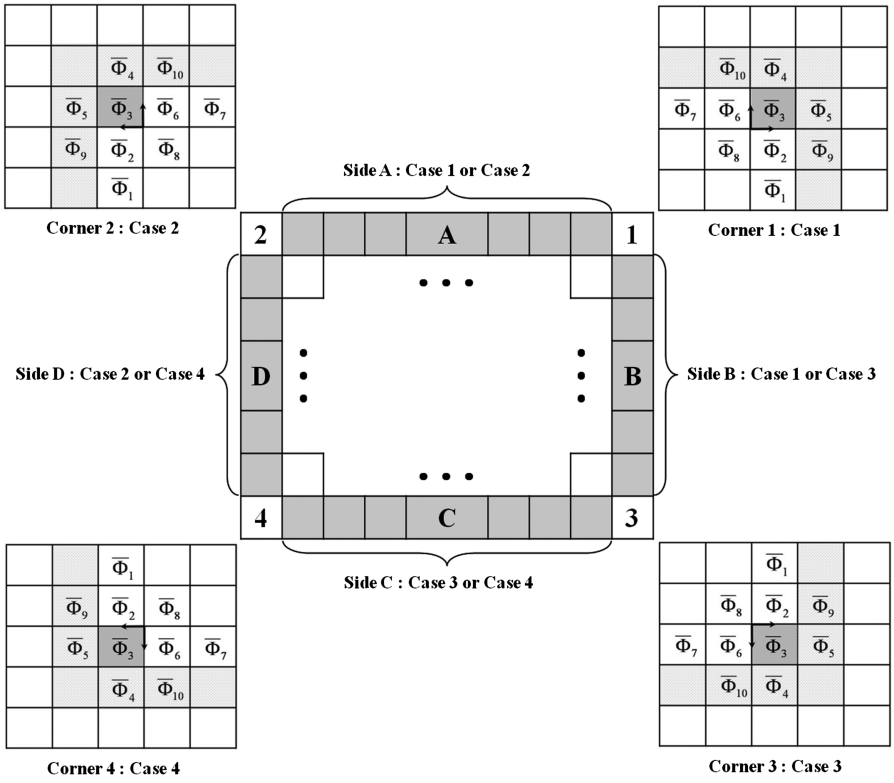

Fig. 7 Stencil at domain boundary.

between continuity and discontinuity in a discretized numerical calculation, whereas the mathematical distinction between them is definite and easy to understand. In the present study, the numerical discontinuous region is defined as the region where the Gibbs phenomenon is observed within the dotted box, as shown in Fig. 9. Four dark cells located at the corners of the dotted box were defined as check cells $\bar{\Phi}_{\text{check},i}$ for the distinguishing mechanism. $\bar{\Phi}_{m,i}$ was obtained by integrating $\Phi_m(\xi_m, \eta_m)$, the interpolation function of grid 1 in the donor cell, as follows:

$$\bar{\Phi}_{m,i} = \iint_S \Phi_m(\xi_m, \eta_m)\, \mathrm{d}A_i \tag{18}$$

A criterion to distinguish between discontinuous and continuous regions is written next. In a numerical continuous region,

$$s_i = \frac{|\bar{\Phi}_{\text{check},i} - \bar{\Phi}_{m,i}|}{|\bar{\Phi}_{m,i}|} \cong \mathcal{O}(\Delta x^4) \ll \varepsilon \tag{19a}$$

In a numerical discontinuous region,

$$s_i = \frac{|\bar{\Phi}_{\text{check},i} - \bar{\Phi}_{m,i}|}{|\bar{\Phi}_{m,i}|} \geq \varepsilon \tag{19b}$$

where $0.001 \leq \varepsilon \leq 0.01$.

The sensing term s_i is the difference between $\bar{\Phi}_{\text{check},i}$ and $\bar{\Phi}_{m,i}$. If the criterion in Eq. (19a) is satisfied for all four check cells, the fringe cell is determined to be located in a numerical continuous region. Otherwise, it is determined to be located in a numerical discontinuous region. The numerical discontinuous region includes a real discontinuity and a continuous wave with high frequency in a relatively coarse grid.

The value of epsilon is determined empirically by considering the significant digits of normalized values. The epsilon may have a value between 0.01 and 0.001. In the present paper, $\varepsilon = 0.001$ is used as the distinguishing criterion. If epsilon has a small value, it can even detect a weak shock wave, whereas the possibility of determining a continuous wave with high frequency as a numerical discontinuous region is also increased. Then, the MLP may make local extrema of a continuous wave with high-frequency flat. On the other hand, if the epsilon has a large value, the possibility of detecting a shock wave decreases, and sometimes it cannot prevent numerical oscillations in the shock. For reference, when epsilon value is chosen as 0.01, even the weak shock wave that is generated at the freestream Mach number of 1.2 can be detected.

B. Step 2: Application of Multidimensional Limiting Process

The basic concept of MLP is expanded from total variation diminishing and summarized as Eq. (20) [14]. For stable computation in a discontinuous region, all properties must satisfy the following distribution:

$$\bar{\Phi}^{\min}_{\text{neighbor}} < \bar{\Phi} < \bar{\Phi}^{\max}_{\text{neighbor}} \tag{20}$$

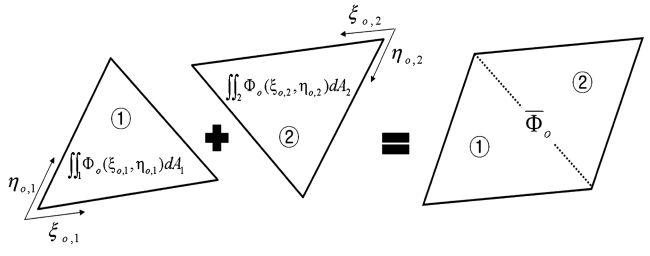

Fig. 8 Integration in the fringe cell of grid 2.

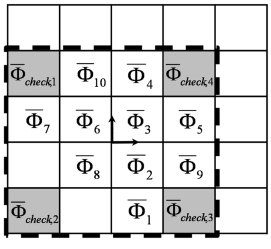

Fig. 9 MLP.

The MLP concept is applied to the present interpolation method as follows. All interpolated values $\bar{\Phi}_o$ in a fringe cell in grid 2 are restricted between minimum and maximum values of neighboring cells in grid 1:

$$\bar{\Phi}^{\min}_{\text{neighbor}} < \bar{\Phi}_o < \bar{\Phi}^{\max}_{\text{neighbor}} \tag{21}$$

where $\bar{\Phi}_o$ is the integrated value in a fringe cell in grid 2, and $\bar{\Phi}^{\min}_{\text{neighbor}} = \min(\bar{\Phi}_2, \bar{\Phi}_3, \bar{\Phi}_6, \bar{\Phi}_8)$ and $\bar{\Phi}^{\max}_{\text{neighbor}} = \max(\bar{\Phi}_2, \bar{\Phi}_3, \bar{\Phi}_6, \bar{\Phi}_8)$ in grid 1.

Once an original interpolated value is restricted by Eq. (21), it locally deteriorates the accuracy of the present interpolation to the second order, in an overall increasing/decreasing region, and to the first order, in local extrema in which a sign of slope is changed.

V. Numerical Result

To investigate the accuracy of the fourth-order interpolation for the overset grid method, numerical calculations of a periodic sine wave and moving vortex problems were carried out. Moreover, a blunt-body problem was solved to see the robustness of the proposed interpolation method in a discontinuous region. Finally, to verify the practicality of the interpolation, the problem of a moving cylinder penetrating through a bubble was calculated.

Basically, the present high-order interpolation method can be combined with all kinds of interpolation schemes such as the second-order MUSCL and WENO, and all kinds of flux schemes such as Roe's FDS and AUSM-type schemes. In the present paper, the M-AUSMPW+ scheme [15] was used for a flux scheme. It controls the advection property of AUSM-type schemes by a pressure-based weight function, which acts as a shock-sensing term. Thus, it can capture a shock wave robustly, with increase of numerical dissipation only in a numerical shock region. In addition, the convective property of M-AUSMPW+ is modified at a cell interface from AUSM-type schemes, and it becomes close to the averaged value of the left and right properties in a continuous region, which makes the spatial accuracy increase by about one order compared with other AUSM-type schemes and Roe's FDS. For an interpolation scheme, MLP5 has the form of the fifth-order interpolation with MLP, named the MLP limiter. In a continuous region, MLP5 is the exact fifth-order polynomial interpolation; thus, it can provide accurate solutions. On the other hand, in a nonlinear discontinuity, the MLP limiter can prevent oscillations from occurring, which makes possible a stable shock capture. Therefore, M-AUSMPW+ combined with the fifth-order MLP5 provides accuracy in a continuous region that corresponds to the sixth-order interpolation method in the present paper. A fourth-order Runge–Kutta scheme was used for the time integration method.

A. Sine Wave

A periodic sine wave, which is a representation of the scalar convective equation, was selected to verify the accuracy of the high-order interpolation. The speed of the sine wave is $M = 0.1$, and the initial density distribution is as follows:

$$\rho = 1 + 0.2\sin(8\pi(x_0 - x)) \tag{22}$$

The grid system used in this problem is shown in Fig. 10b. In the figure, grid 2 is located in the center of grid 1.

The spatial discretization scheme was M-AUSMPW+, with the fifth-order interpolation (MLP5) [13]. The left and right boundary conditions were periodic conditions, and the upper and lower boundary conditions were symmetric conditions. A fourth-order Runge–Kutta scheme with $\Delta t = 0.0001$ was used for time integration.

Two interpolation cases (fourth-order interpolation method and bilinear interpolation method) with three different grid sizes (51×51, 26×26; 101×101, 51×51; and 201×201, 101×101) were tested. The $L2$ norm error in grid 1 for each case was compared at $t = 2$ s. The $L2$ norm error was calculated by comparing with the exact solution.

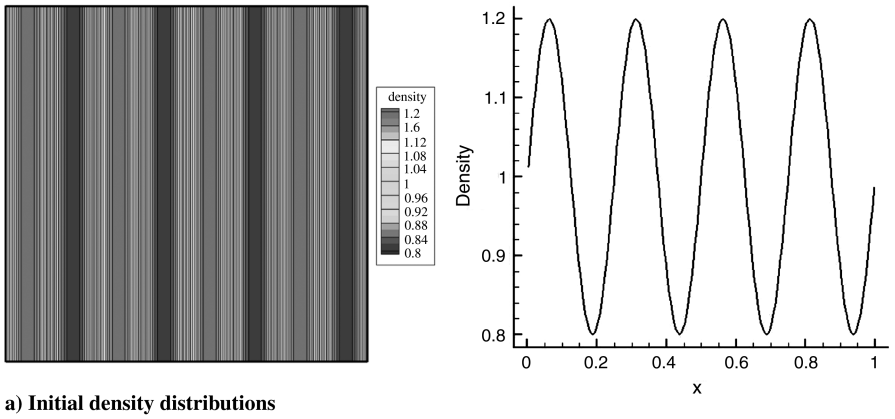

a) Initial density distributions

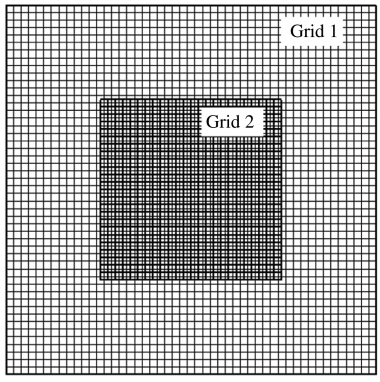

b) Grid system

Fig. 10 Initial condition and grid system.

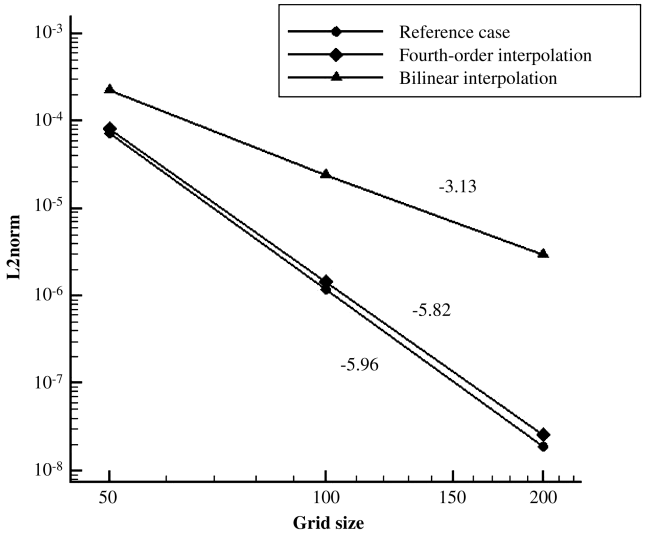

Fig. 11 *L*2 norm error.

The results are shown in Fig. 11 and Table 1. The reference case was calculated without the overset grid method. The slope of reference case was −5.96. In general, the M-AUSMPW+ scheme with the fifth-order interpolation (MLP5) almost produced the result of a sixth-order method, because the M-AUSMPW+ scheme produced a level of accuracy one order higher than the interpolation accuracy in a continuous region [15]. The slope of the proposed interpolation is −5.82, and the bilinear interpolation is −3.13. It is clearly shown that the high-order accuracy was maintained when the proposed interpolation was used with a high-order flow solver. However, bilinear interpolation, which is the second-order spatial accuracy, deteriorated the accuracy from sixth order to third order.

B. Moving Vortex Flow

For the second validation problem, a moving vortex problem was selected to verify the high-order interpolation for the overset grid method in the Euler system equations. The moving speed of the vortex is $M = 0.1$, as shown in Fig. 12.

The initial vortex flow was assumed to have a swirling flow profile with zero net circulation [16,17]. The initial velocity distribution was as follows [18]:

Tangential velocity:

$$u_\theta(r) = M_v \frac{r}{r_v} \exp\left[\frac{1-\varsigma^2}{2}\right] \tag{23a}$$

Radial velocity:

$$u_r = 0 \tag{23b}$$

Vorticity distribution:

Table 1 *L*2 norm error

Grid 1	Grid 2	$L2$ norm
Reference case, slope −5.96		
51 × 51	——	7.138e − 5
101 × 101	——	1.173e − 6
201 × 201	——	1.850e − 8
Fourth-order interpolation, slope −5.82		
51 × 51	26 × 26	8.094e − 5
101 × 101	51 × 51	1.414e − 6
201 × 201	101 × 101	2.527e − 8
Bilinear interpolation, slope −3.13		
51 × 51	26 × 26	2.238e − 4
101 × 101	51 × 51	2.387e − 5
201 × 201	101 × 101	2.929e − 6

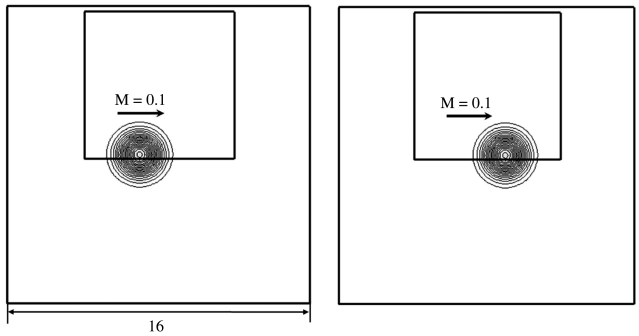

a) Density contours at t=0 s **b) Density contours at t=20 s**

Fig. 12 Density contours.

$$\omega(r) = M_v(2 - (r/r_v)^2) \exp\left[\frac{1-\varsigma^2}{2}\right] \tag{23c}$$

where $\varsigma = \sqrt{(x-x_c)^2 + (y-y_c)^2}/r_v$, (x_c, y_c) is the location of the vortex core, and r_v is 1.0 as the vortex core radius.

The maximum Mach number was $M_v = 0.39$, and the flow was assumed to be isentropic. The initial distributions of the velocity, density, and pressure are expressed by

$$u_0(x,y) = -M_v \frac{y}{r_v} \exp\left[\frac{1-\zeta^2}{2}\right] \tag{23d}$$

$$v_0(x,y) = M_v \frac{x}{r_v} \exp\left[\frac{1-\zeta^2}{2}\right] \tag{23e}$$

$$\rho_0(x,y) = \left[1 - \frac{\gamma-1}{2} M_v^2 \exp(1-\varsigma^2)\right]^{\frac{1}{\gamma-1}} \tag{23f}$$

$$p_0(x,y) = \frac{1}{\gamma}\left[1 - \frac{\gamma-1}{2} M_v^2 \exp(1-\varsigma^2)\right]^{\frac{\gamma}{\gamma-1}} \tag{23g}$$

where $\gamma = 1.4$.

The spatial discretization scheme was M-AUSMPW+, with the fifth-order discretization (MLP5) [13]. Extrapolation was used for the boundary conditions in all directions. A fourth-order Runge–Kutta scheme with $\Delta t = 0.001$ was used for time integration.

Two interpolation cases (fourth-order interpolation method and bilinear interpolation method) with three different grid sizes (51 × 51, 26 × 26; 101 × 101, 51 × 51; and 201 × 201, 101 × 101) were tested.

The $L2$ norm error was calculated by comparing with the solution of the reference case obtained without the overset grid method, to clearly show the error generated only by the overset grid method. Figure 13 and Table 2 show similar results for the sine wave problem. The slope of the proposed interpolation is −5.55, and the bilinear interpolation is −3.39. The proposed interpolation can maintain high-order accuracy, even in the Euler equations.

C. Blunt Body

The third validation problem is a blunt-body problem. Its purpose is to check the robustness of the proposed interpolation method, containing the oscillation removal process in a discontinuous region. $M_\infty = 16.32$ was given for the freestream condition, and, therefore, a strong shock wave occurred in front of the blunt body. When grid 2 was located in the shock area, as shown in Fig. 14, oscillations were generated by the high-order interpolation. To remove these oscillations, MLP was applied in the proposed interpolation.

The conditions for the computation were as follows: 1) spatial discretization [M-AUSMPW+ with fifth-order discretization (MLP5) [13]]; 2) time integration (fourth-order Runge–Kutta method with CFL = 0.4); and 3) interpolation for overset grid method

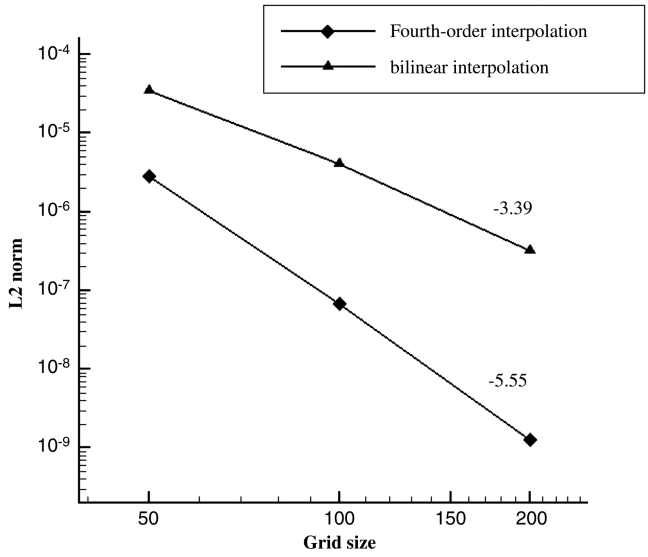

Fig. 13 *L*2 norm error.

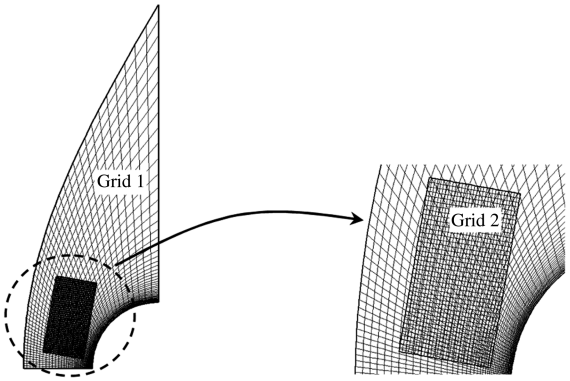

a) Grid system for blunt body **b) Grid 2 in overlapping region**

Fig. 14 Grid system for blunt body.

[fourth-order interpolation without limiting process and fourth-order interpolation with limiting process (MLP)].

Grid 2, including the shock-wave region, was intended to not be aligned with grid 1, to show the robustness of the proposed interpolation method, as shown in Fig. 14. Figure 15c is the result of the

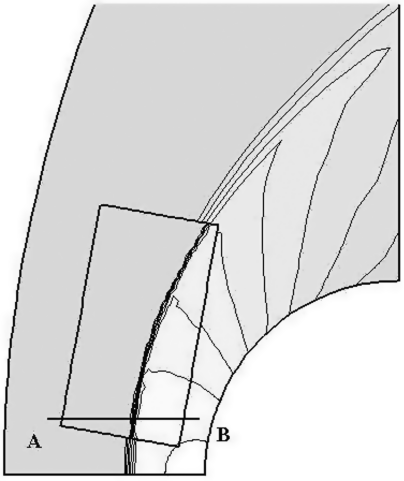

a) Fourth-order interpolation with MLP (17700 iteration)

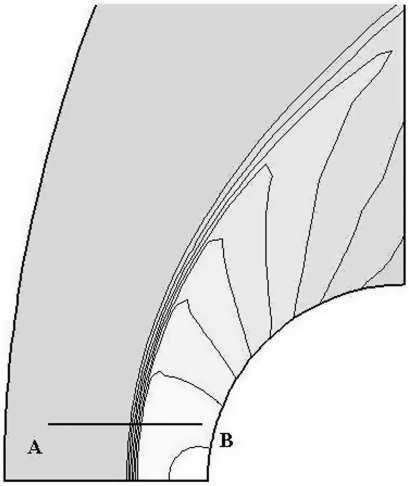

b) Reference case (16500 iteration)

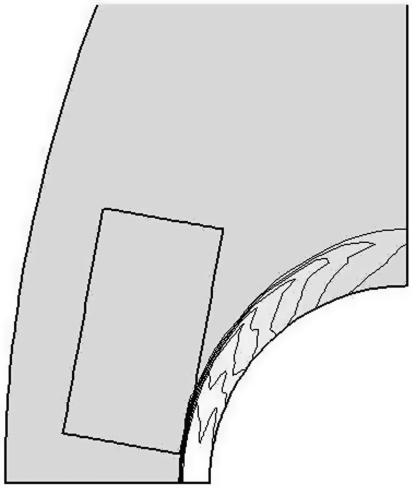

c) Fourth-order interpolation without MLP (717 iteration)

Fig. 15 Pressure contours.

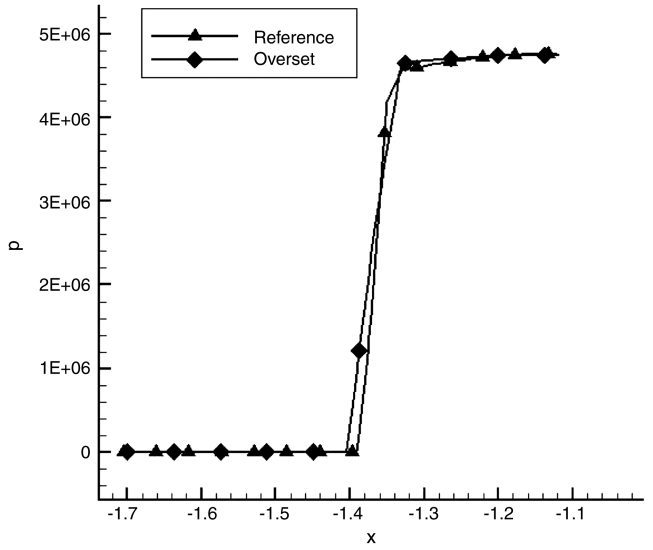

Fig. 16 Pressure distributions along line *AB*.

fourth-order interpolation without MLP, and Fig. 15a is the result of the fourth-order interpolation with MLP. Figure 15b shows the result of the reference case, which was solved using MLP5 without the overset grid method. The fourth-order interpolation without the oscillation removal process diverged as soon as the numerical shock wave contacted grid 2, because the generated oscillations by the high-order interpolation in a discontinuous region had a bad effect on stability, as shown in Fig. 15c. In contrast, the fourth-order interpolation with MLP, the oscillation removal process, captured the numerical shock wave in a stable manner, as shown in Fig. 15a. The pressure contour in grid 2 seemed to wiggle, because grid 2 did not align with the shock wave. However, the pressure distribution along line *AB* in Fig. 16 shows that the proposed interpolation method can capture the shock wave without oscillation.

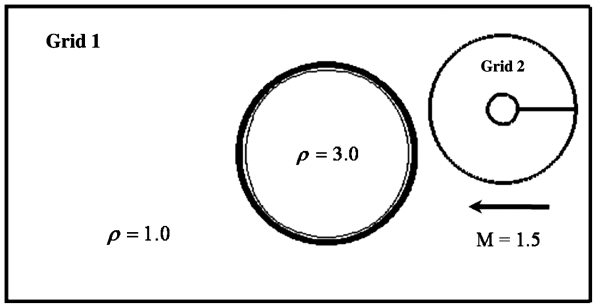

Fig. 17 Initial condition.

D. Moving Cylinder Penetrating Through a Bubble

The last validation problem is a moving cylinder penetrating through a bubble. This problem was chosen to verify the efficiency of the proposed interpolation method for the overset grid system. The result of the proposed interpolation method is compared with a widely used bilinear interpolation method with a conventional second-order scheme.

The bubble is located at the center of grid 1. The density of the bubble is three times greater, as shown in Fig. 17. The cylinder penetrated through the bubble from right to left. The speed of the cylinder is $M = 1.5$.

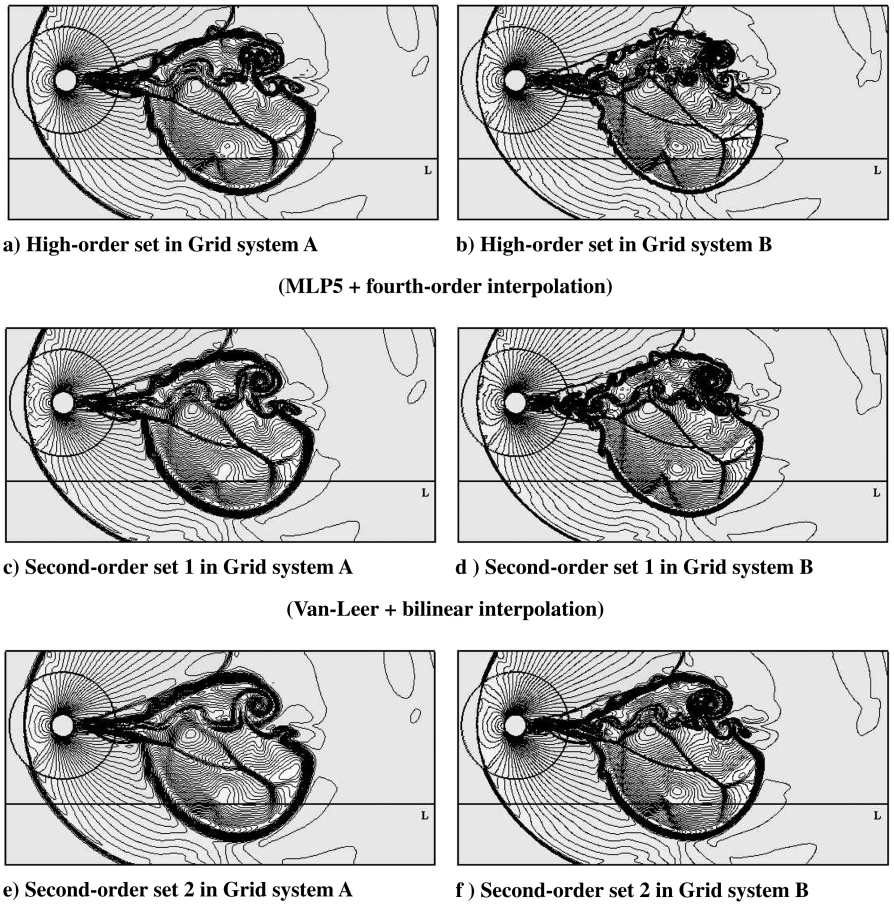

a) High-order set in Grid system A **b) High-order set in Grid system B**

(MLP5 + fourth-order interpolation)

c) Second-order set 1 in Grid system A **d) Second-order set 1 in Grid system B**

(Van-Leer + bilinear interpolation)

e) Second-order set 2 in Grid system A **f) Second-order set 2 in Grid system B**

(minmod + bilinear interpolation)

Fig. 18 Density contours at $t = 9$ s.

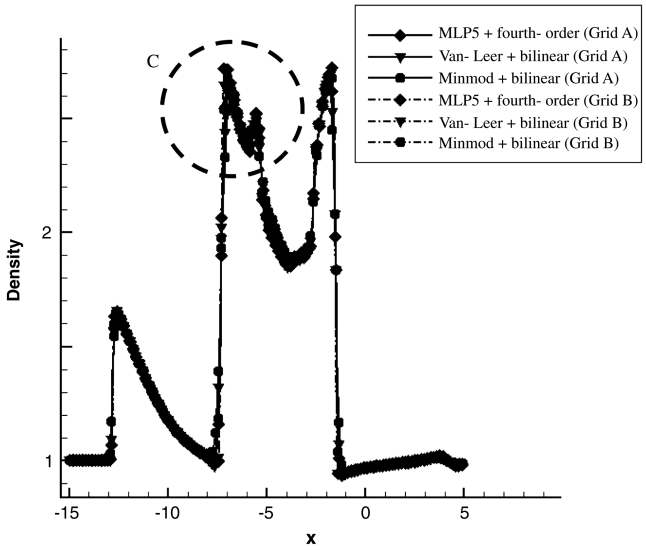

a) Density distributions along line L

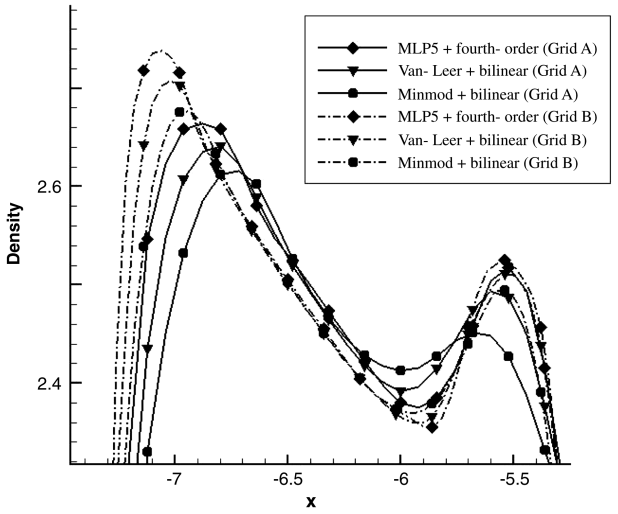

b) Density distributions in region C

Fig. 19 Density distributions along line *L*.

A high-order set and two conventional second-order sets were tested, to compare the efficiency. The proposed interpolation method with MLP5 for the overset grid method was selected for the high-order set. For the conventional second-order sets, the second-order Van Leer limiter and second-order minmod limiter with the bilinear interpolation were selected. The following summarizes the characteristics of the methods used. For the high-order set, fifth-order discretization with MLP (MLP5) [13] (spatial discretization) and fourth-order interpolation with MLP (interpolation for the overset grid method) were used. For the conventional second-order set 1, second-order discretization with Van Leer limiter (spatial discretization) and bilinear interpolation (interpolation for the overset grid method) were used. For the conventional second-order set 2, second-order discretization with minmod limiter (spatial discretization) and bilinear interpolation (interpolation for overset grid method) were used.

Table 2 *L*2 norm error

Grid 1	Grid 2	*L*2 norm
Fourth-order interpolation, slope −5.55		
51×51	26×26	2.784e − 6
101×101	51×51	6.702e − 8
201×201	101×101	1.271e − 9
Bilinear interpolation, slope −3.39		
51×51	26×26	3.486e − 5
101×101	51×51	4.0259e − 6
201×201	101×101	3.184e − 7

Table 3 Computation time

Grid	Flow solver, s	Donor search, s	Flow solver, s	Interpolation, s
		High-order set		
A	2.06	0.20	1.80	0.06
B	9.26	1.56	7.58	0.12
		Second-order set 1		
A	1.24	0.20	1.02	0.02
B	5.67	1.56	4.08	0.03
		Second-order set 2		
A	1.22	0.20	1.00	0.02
B	5.59	1.57	3.99	0.03

The time integration is the fourth-order Runge–Kutta method, with $\Delta t = 0.001$.

Each case was calculated for two different grid sizes: grid system A ($251 \times 151, 51 \times 201$) and grid system B ($501 \times 301, 101 \times 401$). Grid system *B* (dense grid system) had four times more grid points than grid system *A* (coarse grid system).

Figure 18 shows the density contour at $t = 9$ s. Figures 18a and 18b show the results of the high-order set. Figures 18c–18f show the results of the conventional second-order set 1 and set 2, respectively. After the cylinder passed through the bubble, a complex wake structure was generated behind the cylinder. The high-order set produced less of a smearing result than the low-order set in capturing the shock discontinuity and the bubble interface for the same grid, as shown in Fig. 18. To confirm this in detail, the density distributions along line *L* are shown in Fig. 18. The regions in circle *C* in Fig. 19a are magnified in Fig. 19b. The result of the high-order set (MLP5 plus fourth-order interpolation) in grid system *A* has similar peak densities and increasing/decreasing slopes, compared with the result of the second-order set 2 (minmod plus bilinear interpolation) in grid system *B*. Even though the high-order set in grid system *A* was calculated with one-quarter the number of grid points, it showed similar solutions compared with the second-order set 2 in grid system *B*.

Computation times are compared in Table 3. The times were normalized to the flow solver times of the second-order set 2. As the number of grid points increased fourfold, the time for the flow solver increased fourfold. Donor search and interpolation time increased by eight times and two times, respectively, because the number of cells for donor search and interpolation increased eight times and two times, respectively. The flow solver and donor search process were dominant. On the other hand, the time for interpolation was negligible. Even when the high-order interpolation method was used instead of bilinear interpolation, there was little difference in overall computation time. Comparing the computation time of the high-order set in grid system *A* with that of second-order set 2 in grid system *B*, the high-order set took one-quarter the time and yielded a similar solution.

VI. Conclusions

To maintain high-order accuracy for the overset grid method with the high-order flow solver, the high-order interpolation for the overset grid method was developed based on FVM. To solve the coexisting problems of continuous and discontinuous regions, an oscillation removal process (MLP) was introduced. In the sine wave and moving vortex problems, the slopes of the *L*2 norm error of the proposed interpolation were −5.82 and −5.55, respectively, which shows that the proposed interpolation can maintain high-order accuracy in the scalar convective and Euler equations. In the blunt-body problem, the robustness of the interpolation method was examined. High-order interpolation without the oscillation removal

process became unstable as soon as the numerical shock wave contacted grid 2. However, the proposed interpolation method (MLP) for oscillation removal was able to solve the strong shock wave in a stable manner. In the problem of a moving cylinder penetrating through a bubble, the proposed interpolation method with MLP5 showed the effect of a fourfold decrease in the number of grid points, compared with conventional interpolation with the second-order minmod scheme. Because the computational requirements of the interpolation process were very small, with respect to the overall process, the overall computation time showed no difference. Thus, the proposed interpolation method with MLP5 was able to solve continuous and discontinuous regions' coexisting problems in a practical manner, with one-quarter the grid size and one-quarter the computation time compared with the second-order minmod scheme.

Acknowledgment

This research was supported by the National Space Laboratory program through the Korea Science and Engineering Foundation, funded by the Ministry of Education, Science and Technology (2010-0015076).

References

[1] Benek, J., Steger, J., and Dougherty, F., "A Flexible Grid Embedding Technique with Applications to the Euler Equations," AIAA Paper 1983-1944, 1983.

[2] Benek, J., Bunning, P., and Steger, J., "A 3-D Chimera Grid Embedding Technique," AIAA Paper 1985-1523, 1985.

[3] Dougherty, F., and Kuan, J., "Transonic Store Separation Using a Three-Dimensional Chimer Grid Scheme," AIAA Paper 1989-0637, 1989.

[4] Chiu, I., and Meakin, R., "On Automating Domain Connectivity for Overset Grids," AIAA Paper 1995-0854, 1995.

[5] Meakin, R., "Object X-Rays for Cutting Holes in Composite Overset Structured Grids," AIAA Paper 2001-2537, 2001.

[6] Wang, Z., Parthasarathy, V., and Hariharan, N., "A Fully Automated Chimera Methodology for Multiple Moving Body Problems," AIAA Paper 1998-0217, 1998.

[7] Wang, Z., "A Fully Conservative Interface Algorithm for Overlapped Grids," *Journal of Computational Physics*, Vol. 122, No. 1, 1995, pp. 96–106.
doi:10.1006/jcph.1995.1199.

[8] Zheng, Y., and Liou, M., "A Novel Approach of Three-Dimensional Hybrid Grid Methodology: Part 1. Grid Generation," *Computer Methods in Applied Mechanics and Engineering*, Vol. 192, 2003, pp. 4147–4171.
doi:10.1016/S0045-7825(03)00385-2

[9] Yin, T., and Delfs, J., "Sound Generation from Gust–Airfoil Interaction Using Caa-Chimera Method," AIAA Paper 2001-2136, 2001.

[10] Delfs, J., "An Overlapped Grid Technique for High Resolution Caa Schemes for Complex Geometries," AIAA Paper 2001-2199, 2001.

[11] Sherer, S., and Scott, J., "High-Order Compact Finite-Difference Methods on General Overset Grids," *Journal of Computational Physics*, Vol. 210, No. 2, 2005, pp. 459–496.
doi:10.1016/j.jcp.2005.04.017.

[12] Chesshire, G., and Henshaw, W., "Composite Overlapping Meshes for the Solution of Partial Differential Equations," *Journal of Computational Physics*, Vol. 90, No. 1, 1990, pp. 1–64.
doi:10.1016/0021-9991(90)90196-8.

[13] Kyu, H., and Chongam, K., "Accurate, Efficient and Monotonic Numerical Methods for Multidimensional Compressible Flows, Part 2: Multidimensional Limiting Process," *Journal of Computational Physics*, Vol. 208, 2005, pp. 570–615.
doi:10.1016/j.jcp.2005.02.022

[14] Sung-Hwan, Y., Chongam, K., and Kyu-Hong, K., "Multidimensional Limiting Process for Three-Dimensional Flow Physics Analyses," *Journal of Computational Physics*, Vol. 227, No. 12, 2008, pp. 6001–6043.
doi:10.1016/j.jcp.2008.02.012.

[15] Kyu, H., and Chongam, K., "Accurate, Efficient and Monotonic Numerical Methods for Multidimensional Compressible Flows, Part 1: Spatial Discretization," *Journal of Computational Physics*, Vol. 208, No. 2, 2005, pp. 527–569.
doi:10.1016/j.jcp.2005.02.021

[16] Ellzey, J., Henneke, M., Picone, J., and Oran, E., "The Interaction of a Shock with a Vortex: Shock Distortion and the Production of Acoustic Waves," *Physics of Fluids*, Vol. 7, No. 172, 1995, pp. 171–184.
doi:10.1063/1.868738.

[17] Inoue, O. and Hattori, Y., "Sound Generation by Shock–Vortex Interactions," *Journal of Fluid Mechanics*, Vol. 380, No. 01, 1999, pp. 81–116.
doi:10.1017/S0022112098003565.

[18] Taylor, G., "On the Dissipation of Eddies," *The Scientific Papers of Sir Geoffrey Ingram Taylor*, edited by G. Batchelor, Meteorology, Oceanography and Turbulent Flow, Vol. 2, Cambridge Univ. Press, Cambridge, England, U.K., 1918, pp. 96–101.

Z. J. Wang
Associate Editor